Simulating the displacement and energy demand imposed by a strainburst near a tunnel

Alex Rigby [a,*], Dmitriy Malovichko [a], Peter K Kaiser [b]

[a] Institute of Mine Seismology, Australia

[b] GeoK Inc., Canada

Abstract

During a strainburst, there is a simultaneous energy and displacement demand placed on the support system. To better understand the evolution of this demand, high-resolution, dynamic, two-dimensional modelling was conducted of self-initiated strainbursting near an isolated circular tunnel. By analysing the results of this modelling, estimates are made of the radial damage propagation velocity (193 m/s) and the duration to form a strainburst notch (4.1 ms) that are consistent with previously reported values. It is shown that surface displacements evolve to equilibrium more slowly than damage propagation, with a duration of 14.1 ms estimated. This is consistent with source durations estimated from seismic data for small strainbursts. It is shown that for the case considered (stiff loading system, no detaching of rock), an energy pulse is generated that leads to a demand path that deviates from the hyperbolic path used in deformation-based support design (for violent strainbursting in a soft mining environment). A parametric study was conducted to quantify the effect of varying the support pressure, depth of burden, and rock mass parameters (stiffness and brittleness). These factors are shown to strongly influence the demand path generated by a strainburst.

Keywords: *strainbursting, ground support, support demand, numerical modelling, seismology*

1 Introduction

When a strainburst occurs around an isolated tunnel, it simultaneously imposes a displacement and energy demand on the support system (Kaiser & Moss 2022). How this demand evolves over the strainburst's duration can affect whether the remnant capacity of the support system is exceeded or not. It is therefore important to understand the dynamics of the strainburst process for the purposes of forensic analysis of damaging events and for support design.

In previous work, Rigby (2023) conducted dynamic three-dimensional modelling of strainbursting around an isolated tunnel. The main focus of this work was to investigate the spatial and temporal evolution of damage around and along tunnels. From a seismic perspective, it was shown that damage in the low-confinement conditions around a tunnel propagates much slower (particularly in the direction radially outwards from the tunnel) than would be expected for high-confinement shear-rupture process.

While these initial results constitute an important step in understanding strainburst dynamics, the time-consuming nature of the three-dimensional simulation limited the resolution and number of models considered. In this paper, we address this by conducting high-resolution, dynamic, two-dimensional modelling of strainbursting around an isolated circular tunnel. The modelling procedure, which builds on that employed by Malovichko & Rigby (2022), is outlined in the context of a reference case in Section 2.

The nature of the modelling conducted here (continuum with a single isolated excavation) means that the results are illustrative of bursting in a stiff environment where the post-peak deformation is controlled by the tunnel size and the rock mass stiffness. Furthermore, the results are only valid for situations where the

---

[*] Corresponding author. Email address: alex.rigby@imsi.org

support system (approximated by an internal radial pressure) prevents debonding and detachment of rock fragments. If the loading system is softer (due to geological structures, the presence of nearby excavations, yielding in pillars, or seismic softening of the rock mass), different, more violent strainbursting behaviour must be expected as reiterated by Cai (2024). Modelling and quantification of strainbursting in softer environments is reserved for future work.

In Section 3, we analyse how the shape/depth of the damaged volume changes during the strainburst and how the displacement, velocity, and kinetic energy of rock within this volume evolve. This analysis is repeated in Section 4 for variants of the reference case to consider the influence of factors such as rock mass properties, support pressure, and the amount of pre-burst damage on the displacement and energy demands.

2   Reference case

2.1   Geometry

A circular tunnel with a radius of 2.5 m has been meshed using TetGen (Hang 2015). This mesh is composed of a single layer of tetrahedra and has a diameter of 50 m. As shown in Figure 1, the tunnel and a further 2.5 m of the surrounding rock mass have a resolution of approximately 10 cm. The mesh then gets gradually coarser moving outward from the tunnel.
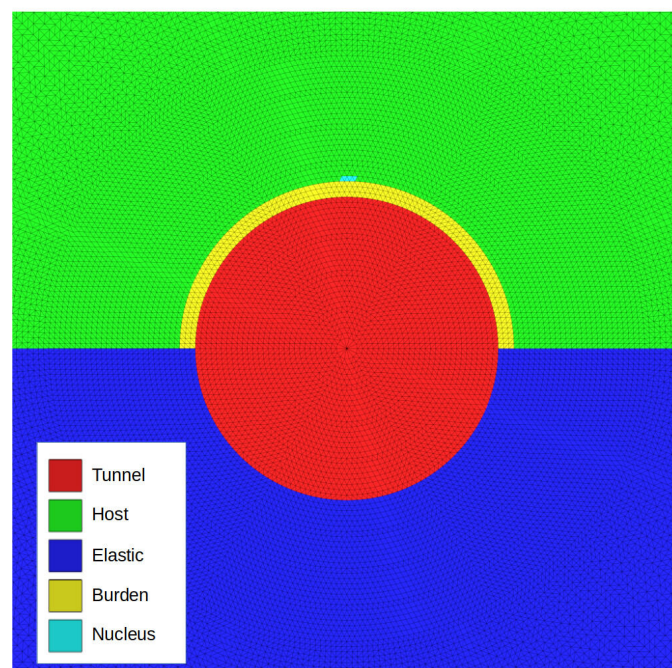
Figure 1   Close-up of tetrahedral mesh around the tunnel. The different regions (colours) are described in Section 2.3

2.2   Loading and support

The minimum in-plane stress of σ_{3p} = 30 MPa is vertical. The maximum in-plane stress σ_{1p} = 50 MPa has been selected such that the maximum induced tangential stress at the surface of the tunnel (120 MPa) is approximately equal to the crack-initiation threshold of the host rock (described in Section 2.3). For the reference case, a support pressure of 125 kPa is applied at the tunnel surface (this corresponds to the centre of the range of reasonable values suggested by Diederichs [2007]).

2.3   Rock mass properties

The rock mass has a Young's modulus of E = 50 GPa and Poisson's ratio of v = 0.25. The inelastic behaviour differs between the regions shown in Figure 1b.

- The bottom/floor half of the tunnel is restricted to elastic behaviour (done to simulate one-sided strainbursting and to simplify later analysis).

- The 'host' rock in the top/back half of the tunnel can yield according to a damage initiation spalling limit (DISL) constitutive model (Diederichs 2007), which is composed of two Hoek–Brown yield surfaces as shown in Figure 2a.

  ○ The intact/peak surface is defined using the values given by Perras & Diederichs (2016) for granite: a uniaxial compressive strength of UCS = 246 MPa, crack-initiation threshold of CI = 125 MPa, and tensile strength of T = CI/8, which gives peak parameters of a_p = 0.25, m_p = 1.05, and s_p = 0.0667 (Diederichs 2007). The residual parameters are a_r = 0.75, m_r = 9, and s_r = 0.001 (Diederichs 2007; Perras & Diederichs 2016).

  ○ For reference, the dashed lines in Figure 2a show approximating Mohr–Coulomb surfaces which have been fitted (Hoek et al. 2002) over the domain $-T \leqslant \sigma_3 \leqslant 30$ MPa. The peak friction angle and cohesion are ϕ_p = 29.2° and c_p = 34.3 MPa , respectively, and the residual values are ϕ_r = 55.9° and c_r = 0 MPa.

  ○ After yield initiation, the Hoek–Brown parameters change linearly as a function of shear plastic strain γ^p until they reach their residual values at a 'critical' shear plastic strain of γ^p_{crit} = 0.2%. At low confinements (to the left of the intersection of the peak and residual surfaces shown in Figure 2a), this constitutes strain weakening/softening, while at high confinements (to the right of the intersection), it constitutes strain strengthening/hardening. The value of γ^p_{crit} = 0.2% was chosen based on the range of 0.1 to 0.3% suggested by Walton (2019) for brittle rock.

  ○ We use the dilatancy model proposed by Zhao & Cai (2010), which provides dilation angle as a function of both shear plastic strain and confining stress σ_3 as shown in Figure 2b. This model requires nine parameters, for which we have used those suggested for granite by Zhao et al. (2010).

- The 'burden' region extends to a depth d_{bdn} = 0.25 m into the back half of the tunnel. It is simulated as an elastic–plastic material with a strength envelope defined by the residual parameters listed above (i.e. a_p = a_r = 0.75 m, m_p = m_r = 9, and s_p = s_r = 0.001) and a fixed dilation angle of ψ = 0°. As described in Section 2.4, it is also manually destressed. These changes (relative to the host rock) are made to introduce a zone of non-dilational burden or baggage that is yielded prior to being loaded by the simulated strainburst.

- The 'nucleus' region extends 0.1 m out from the burden in a 5° angular slice centred in the back of the tunnel. Initially, it has the same material parameters as the host rock, but is then instantaneously weakened by dropping its intact parameters to the corresponding residual values to initiate/nucleate a strainburst as will be described further in Section 2.4.

(a)   (b)
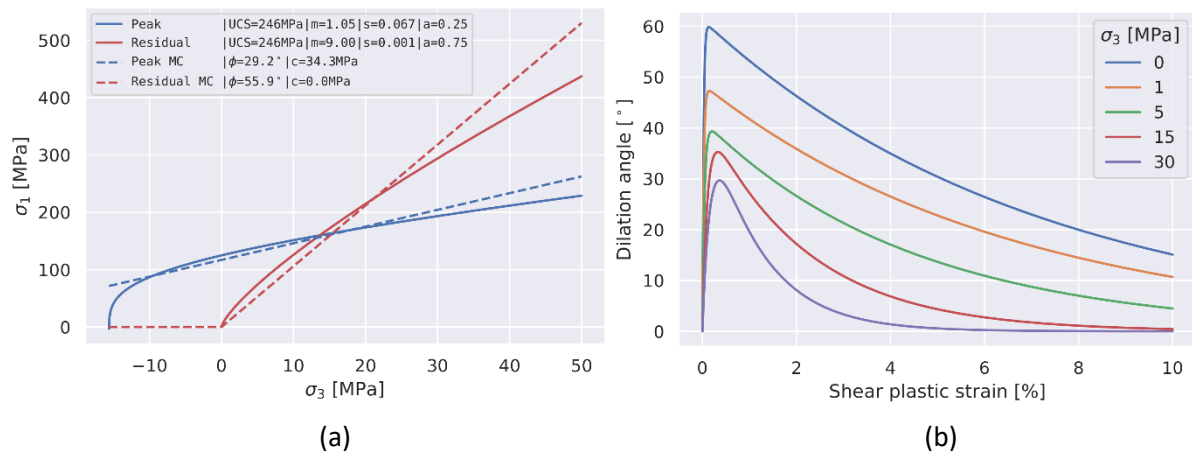
Figure 2   **(a) Peak (blue) and residual (red) yield surfaces defining the damage initiation spalling limit material model used for the host rock. The dashed lines show Mohr–Coulomb approximations; (b) Dilation angle as a function of shear plastic strain for different levels of confinement**

2.4   Simulation procedure

A strainburst behind the burden is simulated using material point method (MPM [Nairn 2003; Basson et al. 2021]) according to the following procedure:

- Each element of the tetrahedral grid described in Section 2.1 is populated with a single particle (material point), which represents a volume of rock. Material properties are assigned to each particle based on the regions outlined in Section 2.3.

- A constant-stress boundary condition is applied according to the loading condition defined in Section 2.2. Particles at the tunnel boundary have an external force applied to simulate an internal support pressure described in Section 2.2. Stress is initially set to zero in the 'burden' region. Stresses and displacements in the remaining regions are initialised according to the analytical solution of Kirsch (1898).

- The pre-strainburst state is obtained by running the model to quasi-static equilibrium with damping applied (Wang et al. 2016).

- To model a self-initiated strainburst, particles in the 'nucleus' region are instantaneously weakened as described in Section 2.3.

- The simulation is then run to equilibrium dynamically with no damping applied within 10 m of the tunnel. Beyond 10 m from the tunnel, gradually increasing damping is applied to avoid reflections.

2.5   Results

Snapshots of the simulated strainburst for the reference case are shown in Figure 3, with particles being coloured by velocity. Over the course of a few milliseconds, the damaged volume (outlined in grey) evolves into the characteristic notch shape as expected for the adopted material model. This damage propagation is accompanied by the release of a pulse of stored strain energy and the radiation of related seismic waves into the surrounding rock mass. Note that the system does not reach equilibrium as soon as the evolution of the damaged volume is complete: it can be seen that particles within this volume continue to move/displace into the excavation over a comparatively longer timescale (tens of milliseconds). A quantitative analysis of these observations is given in Section 3.

The simulated strainburst constitutes a medium-sized seismic event. By comparing the pre-strainburst and post-strainburst states according to the methodology of Malovichko & Rigby (2022), the moment magnitude

can be calculated as $m_{HK} = 0.667\log_{10}L - 0.22$, where L is the extent (in metres) of the source along the tunnel's axis. For L = 3 m, this gives $m_{HK} = 0.10$, while for L = 15 m, it gives $m_{HK} = 0$.
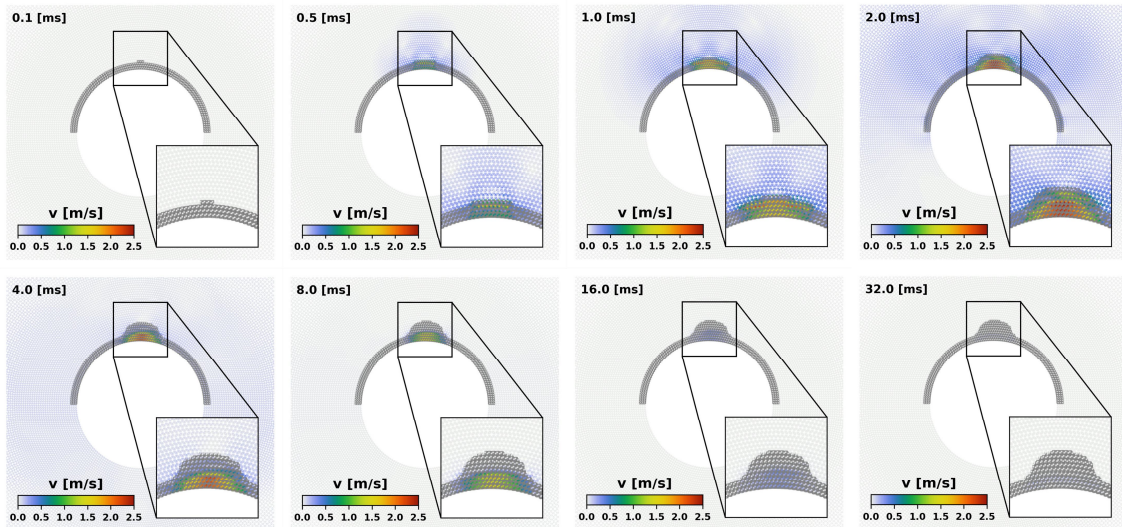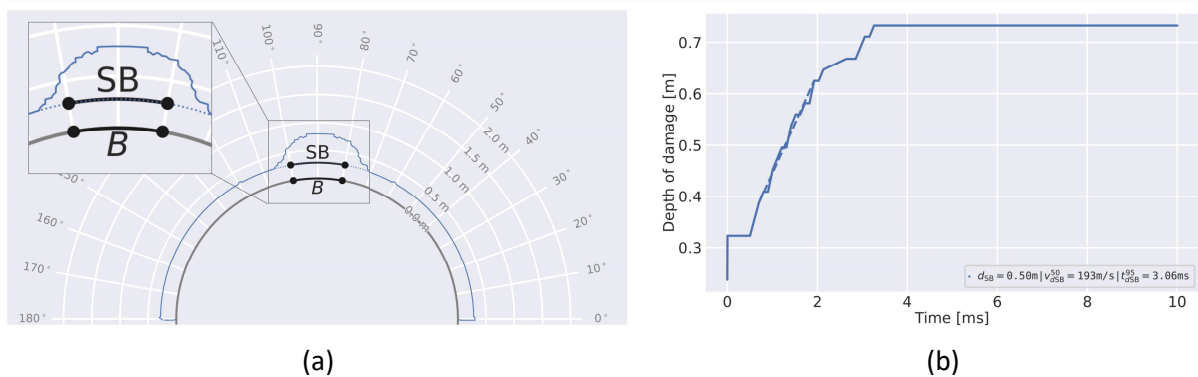

Figure 3   Snapshots of the simulated strainburst for the reference case. Each point represents a particle, which is coloured according to velocity. Those particles that have yielded are outlined in grey. An animated version is available online (Rigby et al. 2024)

3   Analysis

3.1   Damage propagation

We begin by analysing the evolution of the damage volume, which is shown before (dotted line) and after (solid line) the modelled strainburst in Figure 4a. As a function of time, Figure 4b gives the greatest depth of a yielded particle in a 20° slice of the tunnel's back (i.e. from an angle of 80 to 100° as labelled in Figure 4a). The difference between the pre-burst and post-burst depth of damage in this slice is listed in Figure 4b as the depth of strainbursting $d_{SB} = 0.50$ m.

(a)   (b)

Figure 4   (a) Boundary of yielded region before (dotted line) and after (solid line) the simulated strainburst reference case. The black segments labelled 'B' and 'SB' mark the considered portions of the tunnel surface and at the face of the strainbursting volume, respectively; (b) Time history of depth of damage in the back of the tunnel

The radial-propagation velocity is estimated as:

$$v_{d\text{SB}}^{50} = \frac{d_{\text{SB}}/2}{t_{d\text{SB}}^{75} - t_{d\text{SB}}^{25}},$$

(10)

where $t_{d\text{SB}}^{75}$ and $t_{d\text{SB}}^{25}$ are the times taken for the damage increment to reach 75 and 25% of its final value, respectively. Graphically, $v_{d\text{SB}}^{50}$ is the slope of the dashed line shown in Figure 4b, which is equal to the listed value of 194 m/s. Also listed in Figure 4b is $t_{d\text{SB}}^{95}$ = 3.06 m/s, which is the time taken for the depth of damage increment to reach 95% of its final value.

3.2   Ground displacement and velocity

The evolution of the displacement of the damaged volume into the excavation is presented in Figure 5a as time histories of displacement at the surface of the tunnel's back (solid line) and at the face of the strainbursting volume (dashed line). These have been calculated by averaging over the 20° angular segments 'B' and 'SB' shown in Figure 4a. The displacement at the surface reaches a maximum value of u_B = 20.2 mm, while the final displacement at the face of the strainbursting volume is slightly less at u_{SB} = 15.2 mm. This indicates that the burden (pre-yielded volume) continues to dilate as a result of increasing hoop stress over the course of the strainburst. As indicated above, these displacements are realised over a significantly longer time period than that of damage propagation. In particular, as listed in Figure 5a, the time taken to reach 95% of the final displacement at the excavation surface is t_{uB}^{95} = 14.1 ms. The corresponding duration for the face of the strainbursting is similar at $t_{u\text{SB}}^{95}$ = 14.2 ms. These durations are consistent with those estimated for minor to moderate crush-type seismic events based on centroid time by Malovichko (2022, 2023).

Figure 5 shows the time history of ground velocity at the surface and at the face of the strainbursting volume. The maximum values $v_B^{\max}$ = 2.52 m/s and $v_{\text{SB}}^{\max}$ = 2.15 m/s are reached almost simultaneously after just $t_{vB}^{\max}$ = 2.23 ms and $t_{v\text{SB}}^{\max}$ = 1.93 ms, respectively. After this, there is a near-constant deceleration until the system reaches equilibrium. The velocities within the damaged/strainburst volume are roughly one order of magnitude greater than those shown for the surrounding elastic rock mass in Figure 3. In other words, the velocity profile within the burst volume (from the burden to the elastic ground) decreases rapidly, and the average velocity of the burst volume is much smaller (approximately half) than the velocity at the tunnel's surface. It is this average velocity that is used in the methodology of deformation-based support design to assess energy demand (Kaiser & Moss 2022).

The velocity pulse at the excavation surface can cause shotcrete ejection (shotcrete rain) if the tensile strength of the bond (adhesion) is less than the tensile stress generated during the deceleration of the wall. The velocity at the interface of the burden and strainbursting volumes can cause ejection of the burden itself. Note that velocity at which a volume of rock is ejected may be higher than, equal to, or lower than the velocity at this interface. It is equal for thin slivers of rock if there is no momentum transfer from larger blocks. It may be lower if a large volume of rock (e.g. a deep burden) is ejected as a coherent block, and it may be higher if a small volume of rock is ejected by momentum transfer from a large block ($m_1 v_1 = m_2 v_2$).
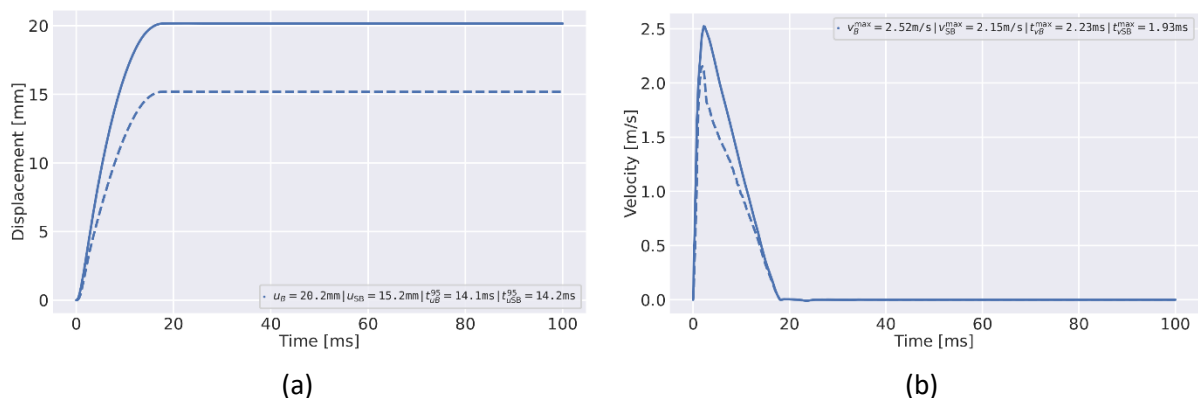
Figure 5   (a) Time history of displacement at the surface (solid line) of the tunnel's back and at the face of the strainbursting volume (dashed line); (b) Velocity time histories with same styling as (a)

3.3 Bulking factor

The bulking factor for a given point in the damaged volume is the ratio of its radial displacement to the depth of damage increment. Figure 6 shows bulking factor time histories for points at the surface of the tunnel and at the face of the strainbursting volume, which reach final values of BF_B = 4.5% and BF_{SB} = 3.4%, respectively. Given that depth of damage evolves much faster than displacement, the shape of the BF time history curves is similar to the displacement curves in Figure 5a.
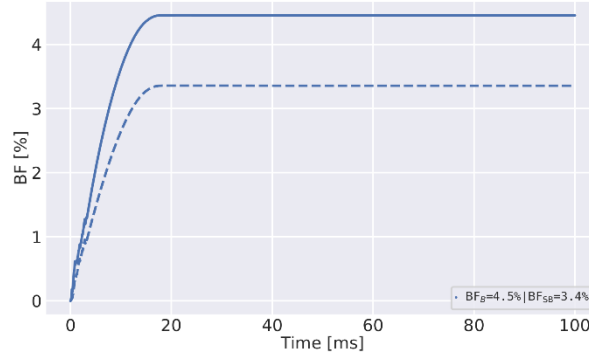
Figure 6 Time history of bulking factor at the surface (solid line) of the tunnel's back and at the point of strainburst initiation (dashed line)

3.4 Kinetic energy pulse

Finally, we consider the kinetic energy density of yielded particles in the 20° angular slice of the tunnel's back as described in Section 3.1. This is calculated as:

$$E_k = \frac{1}{A} \sum \frac{1}{2} m_i v_i^2, \tag{2}$$

where the sum runs over the yielded particles (material points) in the slice, m_i is the mass of the i-th particle, v_i is its radial velocity, and A is the area of the tunnel's surface contained within the slice. For the purposes of interpretation, we make the simplifying assumption that the kinetic energy of the rock as given in Equation 2 is imparted instantaneously (and in full; that is, without any losses to friction, heat, etc. and without allowing fragments to separate) as an energy demand pulse on the support system. Similar to the case of shakedown loading as considered by Malovichko & Kaiser (2020), the actual kinetic energy demand imposed on the support system will be less than that obtained from Equation 2. The values presented here are therefore conservative, with more-accurate quantification of the energy transferred to the support system being reserved for future work.

The time history of the energy demand pulse is shown in Figure 7a (solid line), where it can be seen to rapidly reach a maximum value of E_k^{max} = 2.45 kJ/m² after t_{Ek}^{max} = 1.82 ms before slowly reducing as the system returns to equilibrium. Figure 7a also shows how the kinetic energy is split between particles in the burden region (particles yielded before the strainburst; dotted line) and strainbursting volume (particles that yield during the strainburst; dashed line). The kinetic energy of the burden is greater than that of the strainbursting volume. Note that these values reach their maximum at different points in time, meaning that the listed values of E_{bdn}^{max} = 1.80 kJ/m² and E_{SB}^{max} = 0.68 kJ/m² do not sum to give the maximum total kinetic energy E_k^{max} = 2.45 kJ/m².

Figure 7b shows the same energy pulse plotted as a function of the surface displacement u_B (described in Section 3.2). Such 'demand paths' can be compared with support-system capacity curves to assess whether failure of a given support system is expected (Kaiser & Moss 2022). For the conditions simulated here, the maximum energy demand is reached at a relatively low displacement of u_{Ek}^{max} = 2.64 mm before reducing (approximately linearly) to zero at a displacement of u_B = 20.2 mm. The shape of this demand path is qualitatively (and quantitatively) quite different to the hyperbolic path considered by Kaiser & Moss (2022). This is because the path of Kaiser & Moss (2022) is relevant to cases of violent failure where the loading

system is soft and parts of the rock mass debond/detach as coherent volumes. The continuum modelling conducted here with a stiff loading system (a single isolated excavation) is more consistent with less-violent spalling failure.

In summary, this analysis shows that the stored strain energy released during strainburst propagation may introduce an energy pulse of short duration and relatively small displacements.

(a)   (b)
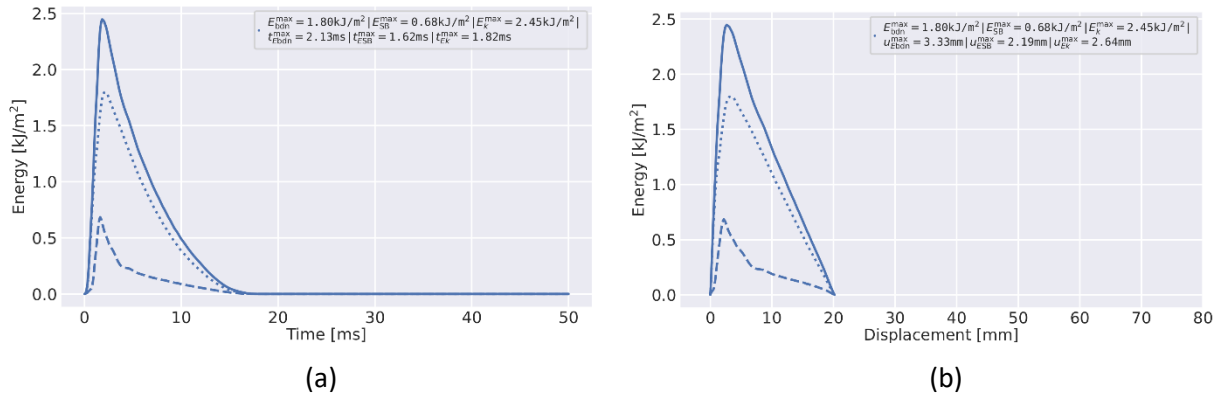
Figure 7   **(a) Time history of the kinetic energy pulse of the burden (dotted line), the strainbursting volume (dashed line), and the total energy (solid line); (b) Displacement–energy demand paths for the same regions**

4   Parametric study

4.1   Support pressure

In this section, we test how variations to the reference case (outlined in Section 2) impact the strainburst dynamics and resulting support demand as analysed in Section 3. This is done one factor/parameter at a time, with all others held constant. First, the effect of changing the reference case's support pressure of 125 kPa to values between 0 and 250 kPa is considered.

It can be seen from Figures 8a and 8b that changes to the internal support pressure have little effect on the shape or time evolution of the notch. This observation is consistent with the results of simulations by Diederichs (2007). Increasing the support pressure from the reference value of 125 kPa results in moderate reductions to displacement (Figure 8c). The effect of reducing support pressure is somewhat more pronounced, with increases to displacement being highest for 62.5 and 0 kPa (this also consistent with the results of Diederichs [2007]). As displacements (u_B and u_{SB}) increase with decreasing support pressure, so do the times required to reach them (t_{uB}^{95} and t_{uSB}^{95}, respectively), which can be interpreted as an increase to the duration of the source process (that the system returns to equilibrium in the 0 kPa case is likely an artefact of the continuum nature of the modelling conducted). Bulking factors follow much the same trend as displacements (Figure 8e). Interestingly, the peak velocities and energies (Figures 8d, 8f, and 8g) are only slightly affected by changes to support pressure. However, increasing support pressure does reduce the duration of the velocity (and, hence, energy) pulse.

We note that the application of a constant support pressure is a very simplistic approach to representing a support system. Therefore, while varying this support pressure has highlighted some interesting/important trends, we cannot expect that the results presented here fully capture the changes in strainburst behaviour resulting from differences in support system. Future work that includes a more accurate/explicit representation of the support system is required to address this gap.
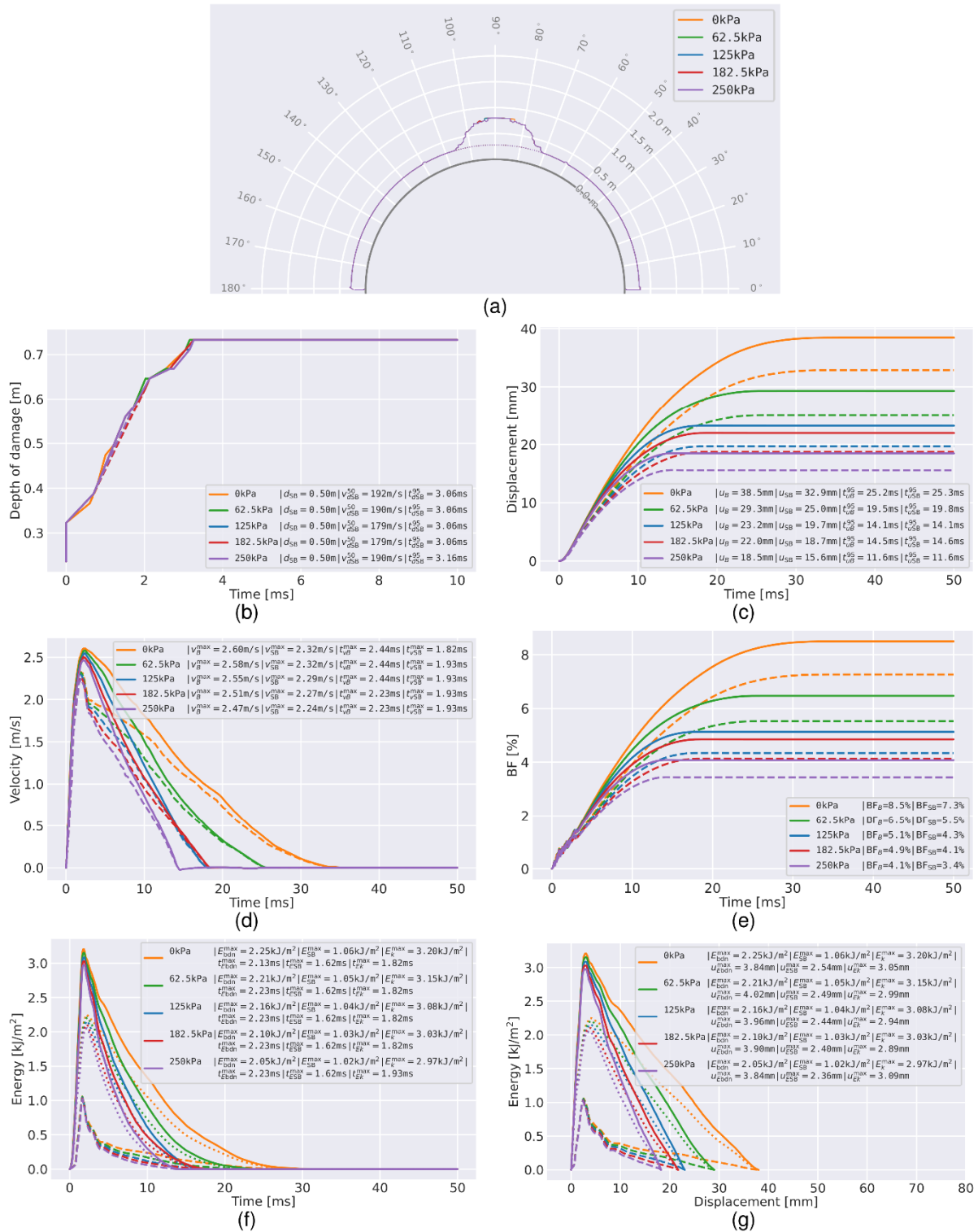
Figure 8 For varying values of support pressure: (a) Boundary of yielded region before (dotted) and (solid) after the strainburst; (b) Time history of strainbursting depth of damage; (c) Time history of surface (solid) and strainbursting volume face (dashed) displacements; (d) Same for velocity; (e) Same for bulking factor; (f) Time history of total (solid), burden (dotted) and strainbursting volume (dashed) kinetic energies; (g) Displacement–energy demand paths for the same regions

4.2   Depth of burden

Next, the effect of altering the depth of burden d_{bdn} between 0 and 0.5 m (0.25 m was used for the reference case) is investigated. As shown in Figure 9a, increasing d_{bdn} causes a widening of the notch that forms during the strainburst. It also results in the notch evolving more slowly (Figure 9b). For the cases of d_{bdn} = 0 m and d_{bdn} = 0.125 m, there is a significant increase in displacement (Figure 9c), while the values for d_{bdn} = 0.25 m, d_{bdn} = 0.375 m, and d_{bdn} = 0.5 m are all similar. A potential explanation for this behaviour is an increase in effective radial pressure at the burden–strainburst boundary with increasing d_{bdn}, which is potentially exaggerated by the continuum nature of the conducted modelling. This pressure is 199, 686, 935 and 1,670 kPa for d_{bdn} = 0.125 m, d_{bdn} = 0.25 m, d_{bdn} = 0.375 m and d_{bdn} = 0.5 m, respectively (obtained by measuring the radial stress in the back of the burden). It can be seen in Figures 9d to 9g that velocities, bulking factors, and energies follow similar trends to displacement (i.e. all increasing substantially as depth of burden reduces).

4.3   Rock mass stiffness

The effect of varying the rock mass stiffness is shown in Figure 10, with values of Young's modulus between 30 and 70 GPa considered (the reference case used 50 GPa). It can be seen in Figures 10a and 10b that the notch gets slightly smaller (in terms of both width and depth) with increasing stiffness. There is a distinct increase in displacement and bulking factor with decreasing stiffness (Figures 10c and 10e) due to the associated increase in hoop straining of the yielded rock inside the notch. There is also an increase in peak ground velocities with decreasing stiffness (Figure 10d), which translates to an increase in peak energy demand (Figures 10f and 10g).

4.4   Strain-softening behaviour

Finally, the effect of varying the critical shear plastic strain is shown in Figure 10, with values ranging from γ^p_{crit} = 0% (i.e. perfectly brittle behaviour) to γ^p_{crit} = 0.8% (the reference case used γ^p_{crit} = 0.2%). Increasing γ^p_{crit} (i.e making the rock mass less brittle) reduces the width and depth of the notch, and results in a significant reduction in the speed at which yielding propagates (Figures 11a and 11b). This can be interpreted as an effect of the less brittle rock mass releasing less energy to sustain strainbursting. Similar reductions with increasing γ^p_{crit} can be seen in terms of displacements, velocities and energies (Figures 11c, 11d, 11f and 11g). Interestingly, although bulking factors also reduce with increasing γ^p_{crit}, they do so in a less pronounced manner given that the trends in strainbursting depth and surface displacement tend to cancel each other out.
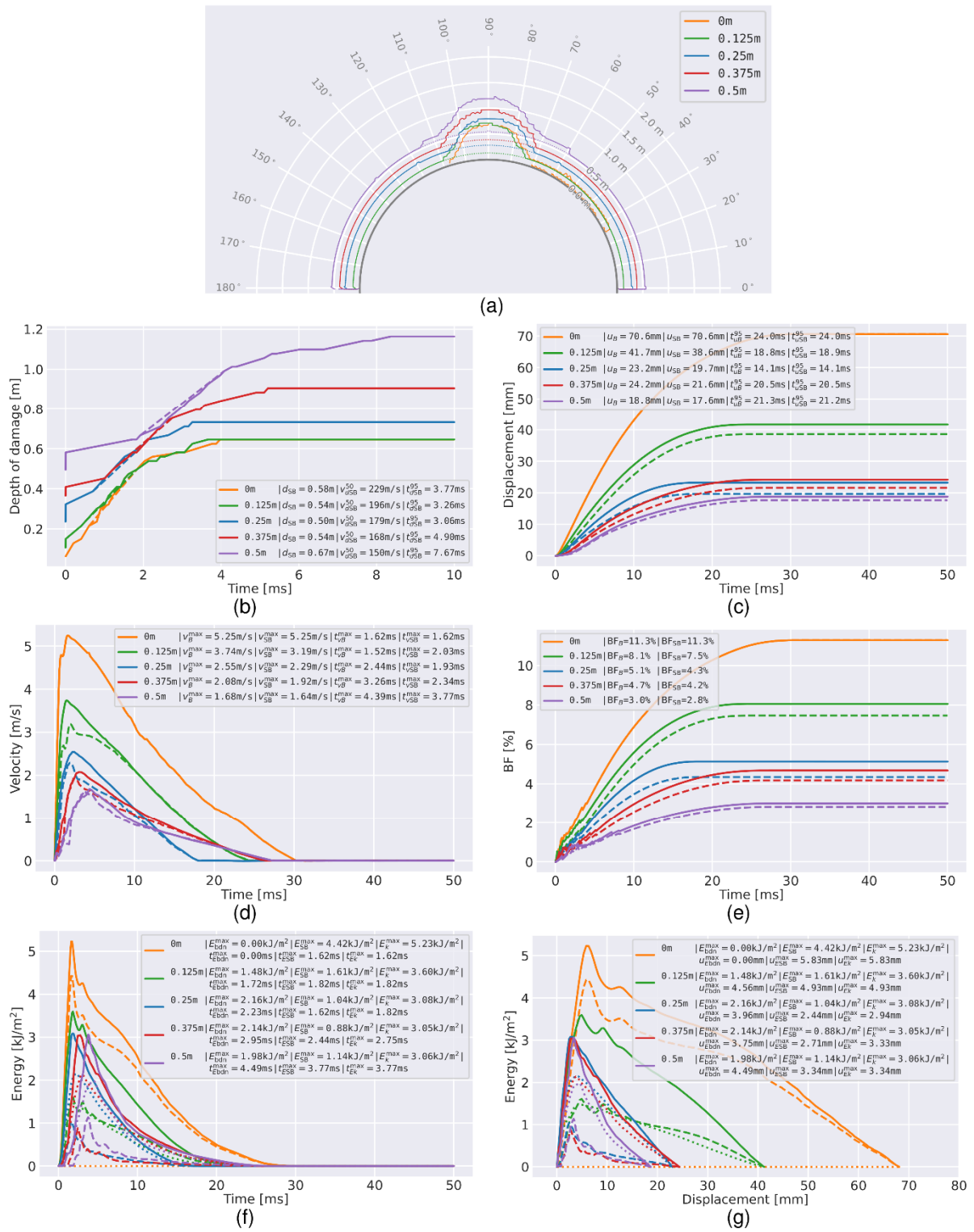
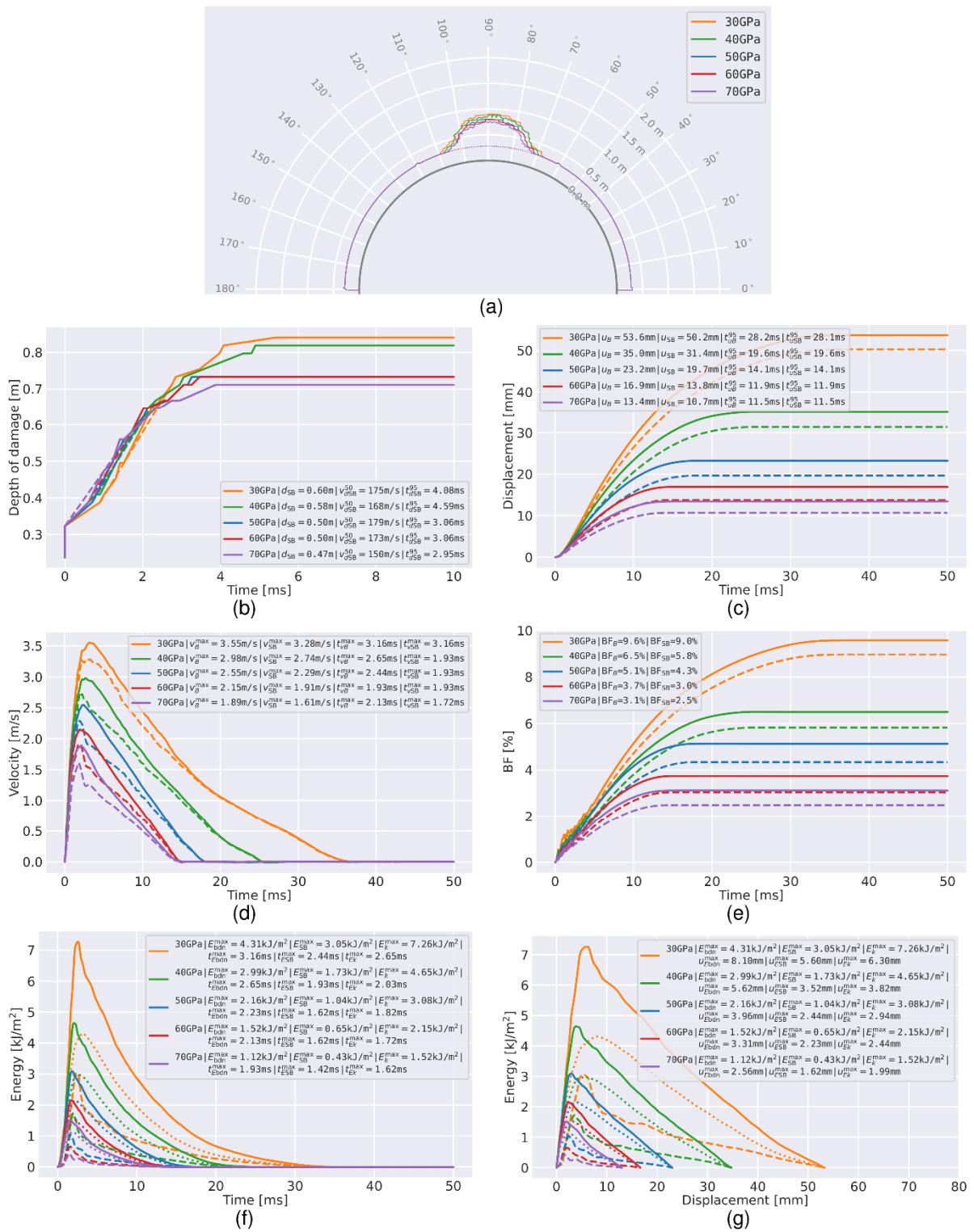**Figure 9   Same as Figure 8 for different depths of burden**

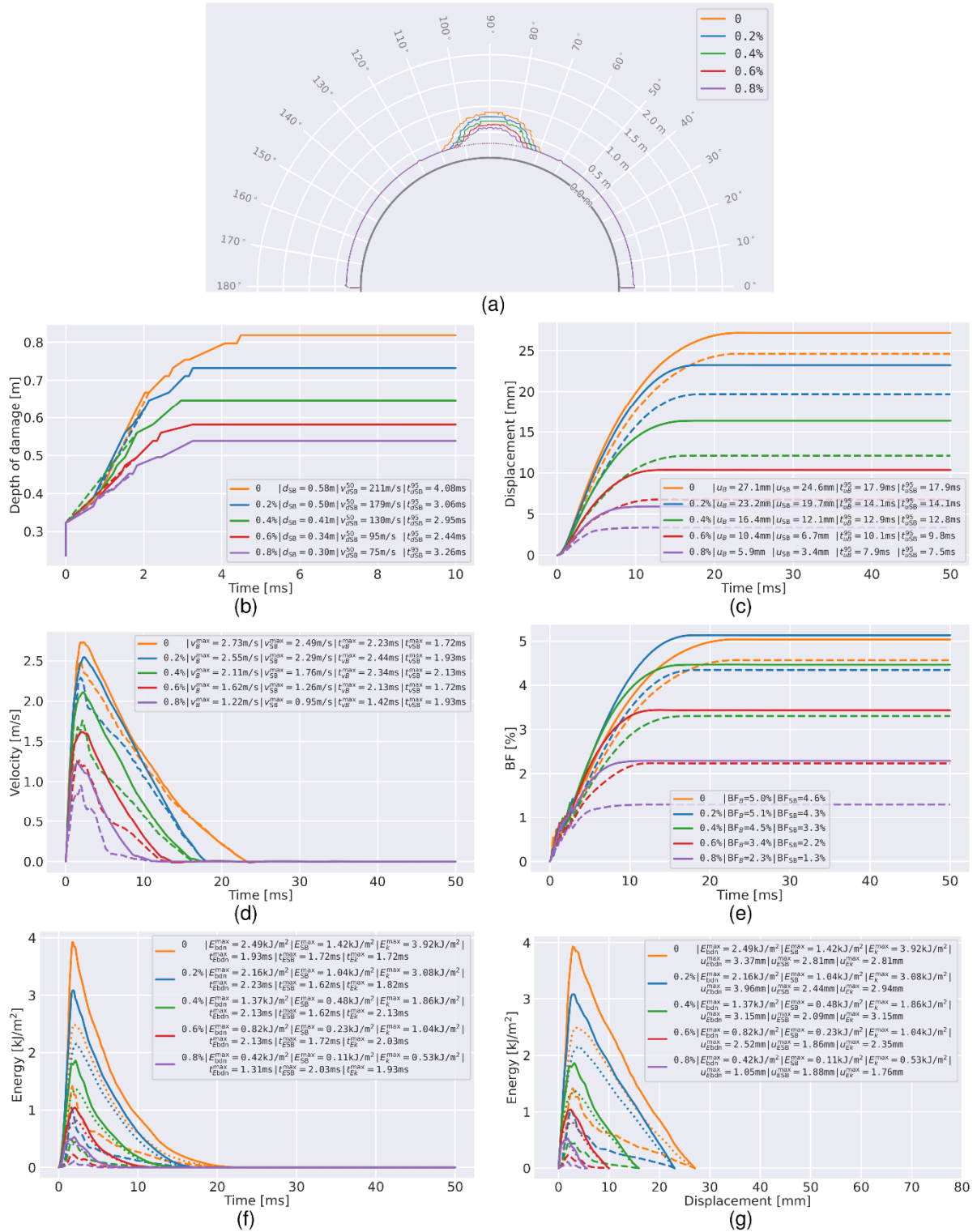**Figure 10   Same as Figure 8 for different material stiffnesses**

Figure 11   Same as Figure 8 for different values of critical shear plastic strain

5   Conclusion

High-resolution, dynamic, two-dimensional modelling was conducted of self-initiated strainbursts near an isolated circular tunnel using the MPM. Under these conditions (a stiff environment without debonding/detaching of rock), the displacement and energy demands are driven by the release of stored strain energy.

The results of this modelling have been analysed in terms of damage propagation, ground displacement/velocity, and energy/displacement demand. Important results derived from this analysis of the reference case include:

- Estimation of a radial damage propagation velocity of 193 m/s and damage propagation duration of 3.06 ms, which is consistent with the values derived from previous three-dimensional modelling (Rigby 2023).

- Estimation of a duration of surface displacement of 14.1 ms (i.e. the time taken for the system to return to equilibrium). This is approximately an order of magnitude greater than the time taken for damage propagation. Furthermore, 14.1 ms is consistent with the lower end of the spectrum of source durations estimated from seismic data (Malovichko 2022, 2023).

- Demonstration that particle velocities within the burst volume are significantly higher (roughly an order of magnitude) than those in the surrounding elastic rock mass.

- Demonstration that for the cases considered, stored strain energy release may create an energy pulse at small displacements. This demand path differs from the hyperbolic path proposed by Kaiser & Moss (2022) (which was derived for the case of violent strainbursting in a soft environment where coherent rock volumes detach and load the support).

A parametric study was conducted to quantify the effect of varying the support pressure, depth of burden, and rock mass parameters (stiffness and brittleness). These factors were shown to quite strongly influence the dynamics of the strainburst.

There are a several directions in which the work presented in this paper can be logically extended:

- The modelling conducted of an isolated tunnel is consistent with bursting in a stiff environment. The influence of system/mine stiffness on strainburst dynamics should be analysed through the inclusion of other excavations or geological features in the model.

- The continuum nature of the MPM modelling means that the effect of rock detaching is not considered. This could be assessed either through performing true discontinuum modelling or by removing particles from the MPM model according to some criteria.

- For the results presented, it was conservatively assumed that the kinetic energy of the bursting rock mass (determined as the sum of individual particle energies) is equal to the energy demand imposed on the support system. This is not necessarily the case and could be investigated in future by incorporating support in a more explicit manner.

- To verify the applicability of the presented modelling results, it would be beneficial to perform a comparison to those from lab/underground testing (e.g. the results of Kasui [2015]).

Acknowledgement

References

Basson, G, Bassom, AP & Salmon, B 2021, 'Simulating mining-induced seismicity using the material point method', *Rock Mechanics and Rock Engineering*, vol. 54, no. 9, pp. 4483–4503, https://doi.org/10.1007/s00603-021-02522-y

Cai, M 2024, 'Rockburst risk control and mitigation in deep mining', *Deep Resources Engineering*, pp. 100019, https://doi.org/10.1016/j.deepre.2024.100019

Diedrichs, MS 2007, 'The 2003 Canadian Geotechnical Colloquium: mechanistic interpretation and practical application of damage and spalling prediction criteria for deep tunnelling', *Canadian Geotechnical Journal*, vol. 44, no. 9, pp. 1082–1116, https://doi.org/10.1139/T07-033

Hang, S 2015, 'TetGen, a Delaunay-Based quality tetrahedral mesh generator', *ACM Transactions on Mathematical Software*, vol. 41, no. 2, pp. 1–36, https://doi.org/10.1145/2629697

Hoek, E, Carranza-Torres, C & Corkum, B 2002, 'Hoek-Brown failure criterion-2002 edition', *Proceedings of NARMS-TAC*, vol. 1, no. 1, pp. 267–273.

Kaiser, PK & Moss, A 2022, 'Deformation-based support design for highly stressed ground with a focus on rockburst damage mitigation', *Journal of Rock Mechanics and Geotechnical Engineering*, vol. 14, no. 1, pp. 50–66, https://doi.org/10.1016/j.jrmge.2021.05.007

Kirsch, EG 1898, 'Die theorie der elastizitat und die bedurfnisse der festigkeitslehre', *Zeitshrift des Vereines deutscher Ingenieure*, vol. 42, pp. 797–807.

Kusui, A 2015, *Scaled Down Tunnel Testing for Comparison of Surface Support Performance*, PhD thesis, Curtin University, Perth.

Malovichko, D 2022, 'Utility of seismic source mechanisms in mining', *Proceedings of the Tenth International Symposium on Rockbursts and Seismicity in Mines*, Society for Mining, Metallurgy & Exploration, Englewood.

Malovichko, D 2023, 'Utilisation of seismic data in the assessment of displacement and energy demand imposed on ground support by strainbursts', in J Wesseloo (ed.), *Ground Support 2023: Proceedings of the 10th International Conference on Ground Support in Mining*, Australian Centre for Geomechanics, Perth, pp. 181–196, https://doi.org/10.36487/ACG_repo/2325_12

Malovichko, D & Kaiser, PK 2020, 'Dynamic model for seismic shakedown analysis', *54th US Rock Mechanics/Geomechanics Symposium*.

Malovichko, D & Rigby, A 2022, 'Description of seismic sources in underground mines: dynamic stress fracturing around tunnels and strainbursting', arXiv, https://doi.org/10.48550/arXiv.2205.07379

Nairn, JA 2003, 'Material point method calculations with explicit cracks', *Computer Modeling in Engineering and Sciences*, vol. 4, no. 6, pp. 649–664, https://doi.org/10.3970/cmes.2003.004.649

Perras, MA & Diedrichs, MS 2016, 'Predicting excavation damage zone depths in brittle rocks', *Journal of Rock Mechanics and Geotechnical Engineering*, vol. 8, no. 1, pp. 60–74, https://doi.org/10.1016/j.jrmge.2015.11.004

Rigby, A 2023, 'Dynamic modelling of strainbursting around tunnels', in J. Wesseloo (ed.), *Ground Support 2023: Proceedings of the 10th International Conference on Ground Support in Mining*, Australian Centre for Geomechanics, Perth, pp. 151–164, https://doi.org/10.36487/ACG_repo/2325_10

Rigby, A, Malovichko, D & Kaiser, PK 2024, *F-SBM-01 Reference Case*, video file, viewed 6 July 2024, youtu.be/dkfkaZiCyR4

Walton, G 2019, 'Initial guidelines for the selection of input parameters for cohesion-weakening-friction-strengthening (CWFS) analysis of excavations in brittle rock', *Tunnelling and Underground Space Technology*, vol. 84, pp. 198–200, https://doi.org/10.1016/j.tust.2018.11.019

Wang, B, Vardon, PJ, Hicks, MA & Chen, Z 2016, 'Development of an implicit material point method for geotechnical applications', *Computers and Geotechnics*, vol. 71, pp. 159–167, https://doi.org/10.1016/j.compgeo.2015.08.008

Zhao, ZG & Cai, M 2010, 'A mobilized dilation angle model for rocks', *International Journal of Rock Mechanics and Mining Sciences*, vol. 47, no. 3, pp. 168–384, https://doi.org/10.1016/j.ijrmms.2009.12.007

Zhao, ZG, Cai, MF & Cai, M 2010, 'Considerations of rock dilation on modeling failure and deformation of hard rocks–a case study of the mine-by test tunnel in Canada', *Journal of Rock Mechanics and Geotechnical Engineering*, vol. 2, no. 4, pp. 228–349, https://doi.org/10.3724/SP.J.1235.2010.00338